# A novel optimized deep learning framework to enhance the image resolution using the radiography

Dr. M. Nagaraju Naik.
Department of Electronics and Communication Engineering
CMR College of Engineering & Technology,
Hyderabad, India

*Abstract:* Digital chest radiography is widely used in healthcare applications since there is no need to store, or film processed with immediate display of images with a lower dose of radiation and thus overcomes some of the issues of film-based radiography. However, the images obtained from the digital flat detector possess less quality to diagnose the disease. A suitable pre-processing technique must be applied for further processing. In context with this, we propose a novel Conditional General Adversarial Network (CGAN) based Rain Fall Optimization (RFO) (CGAN-RFO) approach to enhance the contrast of the images obtained from the digital chest radiography. Prior to the enhancement application Min-Max approach is used for the normalization of raw images which can be used to adapt the intensity of images dynamically. Subsequently, the proposed approach is used to correct the small detailing, contrast, and textures of the subjected images. experimental analyses are made and compared with state-of-art works and show that the proposed work can be used for the effective enhancement of the image contrast for the prediction of diseases from the radiography images.

*Keywords: Conditional GAN, Rainfall optimization, intensity, contrast, normalization, radiography, and digital chest radiography.*

## 1. Introduction

Radiography [1] is an imaging technique for images of the human body, vessels, bones, and organs. The trained person can only diagnose and study the images. The doctors who only can study and explain the scanned images are known as radiologists [2]. Imaging tests done by medical technicians are termed, radiographers. The quality of the image is increased and the noise and radiation are increased. The number of pixels is calculated by the resolution [3] of an image. The total number of pixels, height, and width are identified by the resolution of an image.

The high resolution results in 300 pixels per inch. In this resolution, the quality of printed materials and hard copies requires good quality. The resolutions are divided into spatial, lateral, axial, and contrast resolutions. In the spatial resolution [4], each is determined by sensors and measures the smaller quantity. The ground size is referred to as spatial resolution. Minute images can be seen by spatial resolution. The perpendicular images are by two structures of the lateral resolution. The minimum distance is calculated by the direction of the ultrasound beam and reflectors which is parallel to the beam is denoted as axial resolution [5]. The difference between image intensity is referred to as modality is termed as contrast resolution.

The transfer and the distance function differentiate the distance of contrast and the distance of the image. The factors of x-rays control the quantity and quality of the image. It controls the operator of the factors of the image. The pixels image is determined by pixels per inch [6] (PPI). It performs high quality to create the pixel information. The resolution is denoted in horizontal and vertical measurements. The information is identified by the clarity of the image. The structure of different densities and adjacent images are essential to lower the quality of images. To measure the higher resolution [7] the image quality is resolved to find the visibility of the image from the film, digital, and various images.

 The factors of resolution are special, unanimous, and ordinary resolution.  The major resolution of shareholders is to find a special resolution to modify the organization of images. The extraordinary resolutions affect the resolution of the image for fewer shareholders. The clarity of image in an organization is referred to find the majority of the image quality [8].  The decisions are mentioned by different methods to determine the quality and an image. It removes the unwanted quality and quantity of an image to clear the resolution of information. The number of pixels determines the linear inch and the number of pixels. The linear inch has 72 dots to the resolution of an image. The

quality of the resolution is more and determines the height and width of the image size. It detects the size of the sensor and determines the image quality. The spectral, temporal, and spatial are the sensing factors.

The data directly represent the features of neural networks to use the deep learning methods. The neural network is trained to identify the features of noise [9] in the images and remove unwanted blurring images. It identifies and extracts the features of the image quality. It analyses the picture quality to determine the features of many pictures. It derives information from various parameters and produces clear information from the input images. It reduces cost and radiation, and the picture quality is high. The storage of disk and the capacity of memory cards is more. The state-of-art works were lag in the enhancement of contrast of images for the detection of diseases and in context with this, we proposed a novel CGAN-based RFO algorithm for the radiography image enhancement. The key factors are enclosed below,

> After the acquisition of raw images, the images are normalized by the min-max approach for the conversion of raw images to a required format and removal of noise as much as it can.

> The normalized images are subjected to the proposed CGAN to enhance the intensity of pixels of images and therein increase the contrast. This will help the physician to identify the diseases accurately.

The rest of the work is organized as follows: in section 2 the relevant works are analyzed with their advantages and disadvantages. The proposed methodology is elaborated in section 3. The results and discussion part is enclosed in section 4. The work is concluded in section 5.

## 2. Literature survey

Oh et al. [10] have described a convolutional neural network to analyze the chest X-ray (CXR) radiographs for the diagnosis of Covid-19. The ratio of cardio-thoracic and the intensity distribution in the lung area is used in chest X-rays to examine biomarker images. Segmentation and classification are the two networks to process the algorithm. The chest radiography images are derived to segment the lung and heart profile. The CXR images are classified to test the kinds of diseases. The complexity is low and increases the efficiency, sensitivity, and interpretability. However, the performance of the stated work should be improved for better detection of diseases.

Shi et al. [11] have presented Artificial Intelligence (AI) techniques for image segmentation, diagnosis, and acquisition for Covid-19. The three steps for detecting covid-19 are pre-scan, acquisition, and diagnosis. The protocol that supports and directs the technicians to offer the preparations for pre-scan. The high-quality images are identified by using computed tomography to determine diseases. It is efficient and increases the quality of scans and radiation is decreased. Nevertheless, when the number of data increases and the quality of the output got decreases.

Eslami et al. [12] have implemented a multitask deep learning model for bone-in chest X-ray radiography. The screening and detection are done because the bone structure is clearly seen to detect the diseases. The segmentation process occurs for the visibility of the hidden chest area for suppressing the bones. The parameters are secure and optimize the image-to-image network for prolonged application. It is effective, easier, enhances resolution and the cost is low. Hence, the computational requirements are explored for more variables.

Li et al. [13] have modified a coarse-to-fine CXR bone suppression approach based on unpaired computed tomography. The chest X-ray and computed tomography images are formulated to use the digital radiograph in low resolution. The domain gap is reduced by transferring the digitally reconstructed radiograph to a chest X-ray to increase the network learning. Lung diseases are classified faster, and more efficiently, and resolution is, and computational cost is low. However, the quality should be improved.

Oyelade et al. [14] have stated deep learning and image pre-processing techniques to identify infection of coronavirus. The deep learning and pipelined image pre-processing framework is known as CovFrameNet to classify, measure, and extract the features. It identifies and classifies the computed tomography and chest X-ray images. The coronavirus is classified using stochastic gradient descent (SGD) to produce more accuracy. However, a high volume of chest X-ray images is explored.

Al-Waisy et al. [15] have presented a hybrid deep learning framework named as COVID-CheXNet system from chest X-ray images to identify coronavirus. Image classification, segmentation, fusion, and pre-processing are the steps that take place in the process of the proposed system. To classify and extract the features ResNet34 and HRNet are the two deep learning methods to differentiate the proposed method. The clarity of the image is increased and the noise level is decreased. Thus, the chest X-ray images are explored for larger datasets.

To classify covid-19 Shankar et al. [16] have demonstrated a fusion model hand-crafted with deep learning features (FM-HCF-DLF) model to detect coronavirus. The features are classified and extracted for the fusion model. Gaussian filtering-based pre-processing processes the handcrafted features to validate the dataset. The accuracy, sensitivity, and specificity are more compared with previous techniques. Hence, other classifiers are to be explored.

Karar et al. [17] have described a deep learning framework for identifying coronavirus in X-ray scans. The positive and negative stages are identified by the proposed system. The performance of X-ray images is classified as reliable and selective for the modules. Various classifiers are allowed to classify the images from the datasets. The bacteria and virus are identified in the diagnosis of the coronavirus from X-ray images. It is efficient and decreases the cost. However, the performance of classifiers is enhanced.

## 3. Proposed Methodology

For diagnosing the disease underlying it is necessary to enhance the contrast of the raw images acquired by any kind of modality and here we are using an optimized deep learning-based approach to enhance the radiography images. this approach enhances the contrast and at the same the visibility of the anatomical framework. The schematic structure of the proposed work is illustrated in figure 1. The steps involved in our proposed work are listed below, after acquiring the radiography images the images are normalized using the min-max approach, and henceforth the contrast of the normalized images can be increased using the RFO-CGAN approach. Subsequently, the processed information is stored along with the patient information as Digital Imaging and Communication in Medicine (DICOM) file.
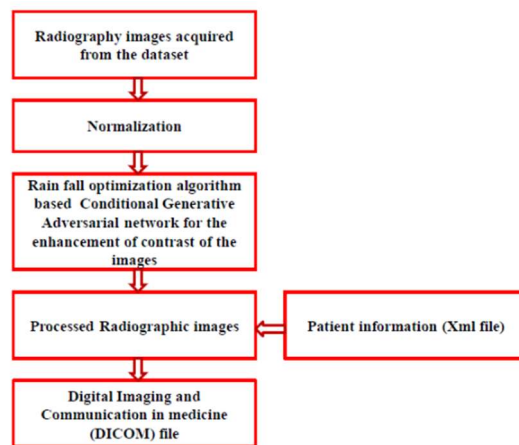


**Fig 1**: Schematic Workflow of proposed work

### 3.1 Min-Max based Normalization

It is the first step [19,20] of our proposed work and the normalization of the images is represented by,

$$I_{Norm}(a,b) = \begin{cases} 2^x - 1 & for \ N(a,b) > 2^x - 1 \\ N(a,b) & for \ 0 \le N(a,b) \le 2^x - 1 \\ 0 & for \ 0 < N(a,b) \end{cases} \qquad (1)$$

Here,

$$N(a,b) = round\left( \frac{I(a,b) - \min_{Norm}}{\max_{Norm} - \min_{Norm}} \left(2^x - 1\right) \right) \qquad (2)$$

The minimum normalized value is denoted as $\min_{Norm}$ and the value of maximum normalized can be given as $\max_{Norm}$ and after normalization the number of image pixels is estimated as x. the minimum and maximum intensities taken from the image histogram are taken as $\min_{Norm}$ and $\max_{Norm}$.

### 3.2 CGAN based RFO for the image contrast Enhancement

For the image contrast enhancement, we have taken the novel conditional GAN due to the limitations of conventional GAN in terms of generator and discriminator networks. It also possesses shortcomings like mode mixing and mode collapsing during the training process which means it is arduous to assure the quality and diversity of the image. To tackle this adoption of the class label and b in both the networks which results in CGAN [21]. This CGAN can be used for the extension of unsupervised GAN to the supervised GAN and also used to reconstruct the defect images, therein averts the mode mixing effect. In this work, we have used DCNN instead of multilayer perceptrons in D and G networks and enhanced the feature extraction process

| **Algorithm 1**: Resampling of proposed CGAN |
| --- |
| Input: Datasets that are imbalanced $Data_{raw}$ <br><br> Output: Dataset that has been processed and balanced $Data_{processed}$ <br> Start <br> For i=1 to TE do <br> For j=1 to 5 do <br> Sample n arbitrary noises that were obtained from the uniformly distributed data <br><br> Sample n arbitrary noises from the original raw data $Data_{raw}$ <br> Fix G and update the D network <br> End for <br> Sample n arbitrary noises that were obtained from the uniformly distributed data <br> Fix D and update the G network <br> End for <br> end <br> Training based resampling procedures by our proposed approach <br> Start <br> For l=1 to e do <br> Initialize the types of the noises being generated <br> End for <br> The newly generated samples are mixed with a raw dataset that is imbalanced <br><br> $Data_{processed}$ <br><br> end |

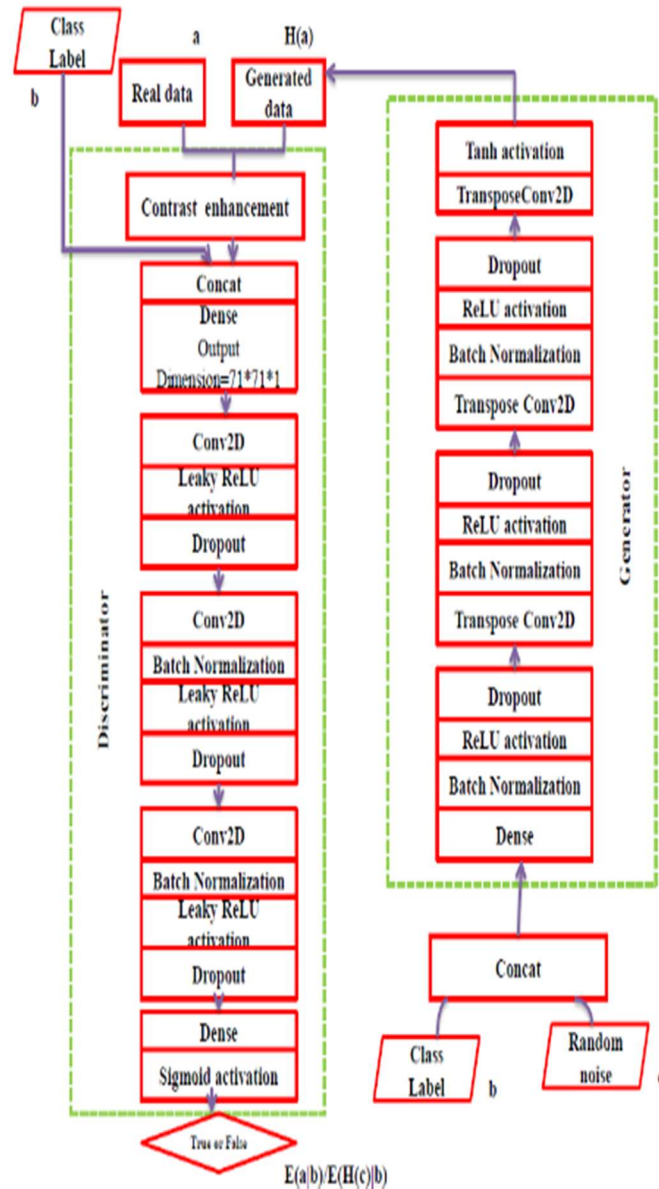[24]. The schematic overlay of the proposed approach is depicted in figure 2.

**Fig 2**: Schematic overlay of proposed CGAN

The contrast enhancement of the D network has been performed on both real and generated data and thus defected regions from the raw low contrast images can be enlightening and thus consequent convolutional operation [18]. Hence the extraction of defect features can be performed exactly in the D network without affecting the contrast of the images in the G network. The two phases in our proposed approach are resampling and training of CGAN. The objective function for the training process and accomplished effect of training and steps involved are shown in algorithm 1.

To increase the contrast further we have introduced an optimized algorithm known as the RFO algorithm which is elaborated on in the following section.

### 3.3 Rain Fall optimization (RFO) algorithm:

During rainfall, the drop behavior inspires the rainfall optimization (RFO) algorithm. Raindrops fall from such a mountain to shape rivers and streams which flow into the ocean or ponds. Since this behavior of rainwater is comparable to the discovery process that is used to discover the minimum standards of a function, this procedure can be done in optimizers [22]. Raindrops would then keep falling till the individuals come to a point in which they can no longer drop.

The following attributes present the rainfall that creates the artificial drop population. At the optimization problem of $j^{th}$ dimension, the raindrop position is denoted as $Y_j$. An active or inactive drop is marked via a status flag. From the global optimum, stuck the drop when the artificial drop is inactive. The following equation calculates the attribute's rank. At $T^{th}$ iteration, the raindrop position is determined via attributes.

$$RD_{Rank}^j = \begin{cases} Rank_T^j = \alpha_1 \times order\left(D1_T^j\right) + \alpha_2 \times order\left(D2_T^j\right) \\ D1_T^j = F\left(E_T^j\right) - F\left(E_1^j\right) \\ D2_T^j = F\left(E^j\right) \end{cases}$$

(3)

At $T^{th}$ iteration, the rate of value change is $D1_T^j$ based on $E^j$ raindrops. The current raindrop is $D2_T^j$. The weighting coefficients $\alpha_1$ and $\alpha_2$ are and in which the range 0.5 is the constant value. At $T^{th}$ iteration, the rank is returned to a raindrop $E^j$.

The next drop position is defined via random search. The neighborhood area is defined based on the property of step size. At $T^{th}$ iteration, the drop speed changes the neighborhood size for stimulating the drop descent from a peak [23]. If it moves to a steeper area when the delta among the last iterations fitness is higher. The terrain slope is inversely proportional to the drop's speed.

$$RD_{Step}^j = \begin{cases} Step_0, & for \ j==0 \\ Step_{j-1} \times (1+S_R), & for \ E_{D_{j-1}}==0 \\ \dfrac{Step_{j-1}}{1+S_R}, & for E_{D_{j-1}} > 0 \end{cases}$$

(4)

For the solution, the parameter of initial step size is $Step_0$. The random value $S_R$ tends to 0 to 1 interval. At the previous iteration, the step size is $Step_{j-1}$ and the explosion counter is $E_{D_{j-1}}$.

The higher quality solution is produced when the raindrop moves slower than in the exploitation stage.

$$M_j^K = C_j^K + \left(M_0^K \times C_{Step}^j\right)$$

(5)

At $k^{th}$ dimension, all drops based on initial neighborhood size are $M_0^K$. The artificial raindrop position is $C_j^K$.

Based on the current iteration, the drop step size is $C_{Step}^j$.

$$M_0^K = \left( \left| U_K \right| + \left| L_K \right| \right) \times 0.02 \tag{6}$$

The below expression generates the raindrop $E^j$ of the neighbor point position is $PM_i^j$.

$$\left\| \left( C_j^K - PM_i^j \right) \overline{\alpha}_K \right\| \le \left\| M_j^K \cdot \overline{\alpha}_K \right\|$$
$$1 \le K \le m$$
$$1 \le j \le n$$
$$1 \le i \le pm \tag{7}$$

Whenever an artificial drop lacks a dominant neighbor peak, the explosion phase is started. This

| Stages | Sample of original images |
|---|---|
| Normal | 190 |
| Abnormal | 220 |
| Total | 410 |

**Table 1:** The example of healthy and unhealthy images

occurs whenever a drop of rain becomes trapped in minima but also when there aren't enough neighbor spots produced.

$$C_j^K = \left[ \left( \left| U_K \right| + \left| L_K \right| \right) \times Base_E \right] \tag{8}$$

The below equation explains the $Base_E$.

$$Base_E = \begin{cases} (0.9)\left(10^{-\exp+b}\right)\left(Ed^{Base_{\exp}}\right), & b \ge 1 \\ (0.9)\left(10^{-\exp+1}\right)\left(Ed^{Base_{\exp}}\right), & b < 1 \end{cases} \tag{9}$$

In the current drop, the number of explosion processes is $Ed$.

$$b = -\log\left( \frac{\left| U_K \right| + \left| L_K \right| \cdot 3/200}{0.9} \right) \tag{10}$$

If the explosion procedure is going around and no dominant position has been found, a drop of rain could become inactivated. Furthermore, higher-rank droplets could indeed interpolate so much during the explosion procedures to become inactive.

After the enhancement of images, the processed images are stored and incorporated with an XML file which contains the patients' information in a DICOM format file. In radiology, these files have a certain format that was accepted by the international medical council and preserves the exact information via the medical images.
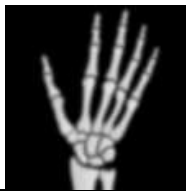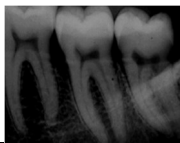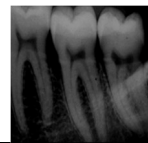
## 4. Experimental result and discussion:

This section discusses the experimental outputs of a novel optimized deep learning framework to enhance the image resolution using radiography. The state-of-art results based on various performance measures validate the performance of the proposed methodology. The 16 GB of RAM, 69 K GPU graphics card, and Windows 10 operating system with the Google Colaboratory server trained and the Python programming language provides the implementation outputs.

### 4.1 Dataset description:

The test was carried out just by obtaining COVID-19 infected X-ray images of individuals again from this data collection supplied by normal X-ray images and Joseph Paul Cohen4. The COVID-19 affected cases have pertained to the 198 X-ray images present in the data collection of COVID-19 images at the time of this study. From Chest X-ray Images (pneumonia) repository, the healthy individuals of 210 X-rays images and virus-affected patients of 198 X-rays images take the COVID-19 data collection, which is suffered from the X-ray images and develops the experimental work. From the 1112× 624 to 2170×1953 pixels ranges, vary the compiled dataset of the original size. Scale all the images into 512×512 pixels for this experimental study. The dataset details used in this study are summarized in Table 1. Table 2 expresses the sample images based on both low and higher resolution.

**Table 2:** Sample images based on their resolution

| Name of the radiography images | Low-resolution images | High-resolution images |
|---|---|---|
| Hand |  |  |
| Skeletal |  |  |
| Tooth |  |  |
| Fingers |  |  |

| | | |
|---|---|---|
| Bone | | |
| Chest | | |
| Brain | | |
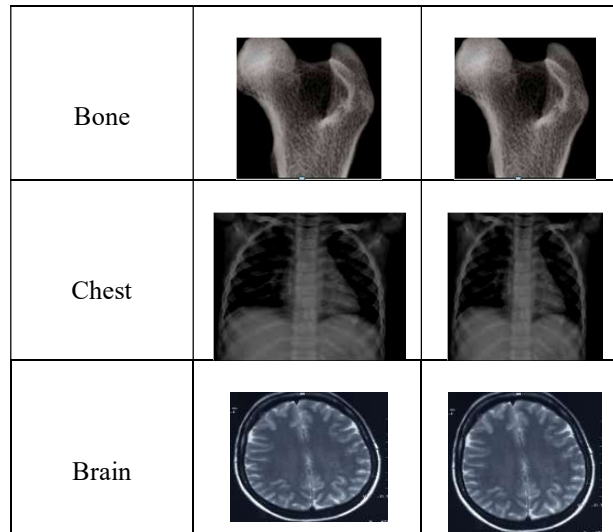
## 4.2 Performance measures:

This section presents various performance measures to validate the performance of a novel optimized deep learning framework to enhance the image resolution using radiography.

$$Accuracy = \frac{T_n + T_p}{F_n + F_p + T_n + T_p} \quad (11)$$

$$\text{Pr}ecision = \frac{T_p}{F_p + T_p} \quad (12)$$

$$Recall = \frac{T_p}{F_n + T_p} \quad (13)$$

$$Specificity = \frac{T_n}{F_p + T_n} \quad (14)$$

$$Sensitivity = \frac{T_p}{F_n + T_p} \quad (15)$$

From the above equation, the falsely positive and negative classes are $F_p$ and $F_n$. Similarly, the true positive and negative classes are $T_p$ and $T_n$.
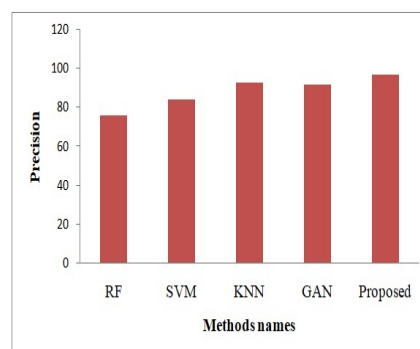
## 4.3 Performance analysis:

Figure 3 explains the evaluation performance of accuracy. Methods like RF, SVM, KNN, GAN, and proposed are used as the comparative methods. We have obtained 80%, 89%, 91%, 95%, and 97% accurate results based on RF,

SVM, KNN, GAN, and proposed methods. However, the proposed method offers superior accuracy results to the previous methods.
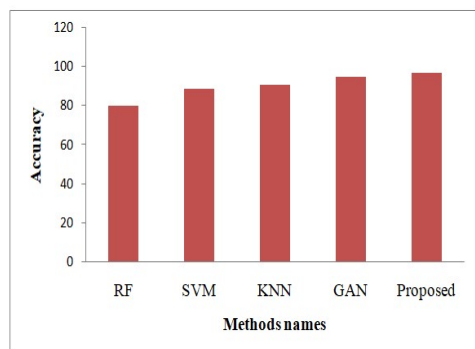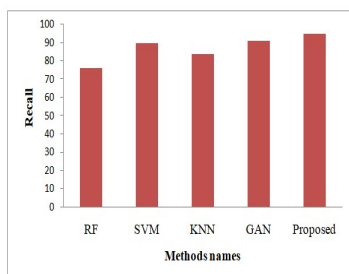



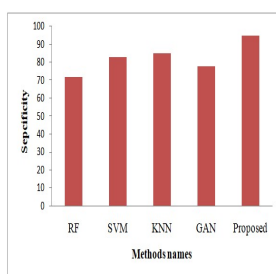**Figure 3:** Performance evaluation of the accuracy          **Figure 4:** Performance evaluation of precision
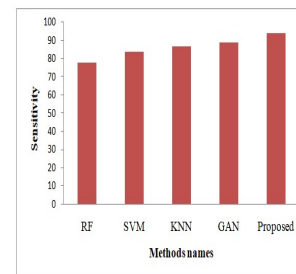
Figure 4 depicts the precision evaluation performance. Comparative methods include RF, SVM, KNN, GAN, and proposed methods. We obtained precision results of 76 percent, 84 percent, 93 percent, 93 percent, and 97 percent using RF, SVM, KNN, GAN, and proposed methods. However, the proposed method outperforms the previous methods in terms of precision.The recall evaluation performance is depicted in Figure 5. RF, SVM, KNN, GAN, and proposed methods are examples of comparative methods. Using RF, SVM, KNN, GAN, and proposed methods, we obtained recall results of 76 percent, 90 percent, 84 percent, 91 percent, and 95 percent. However, in terms of recall, the proposed method outperforms the previous methods.





**Figure 5:** Performance evaluation of recall

**Figure 6:** Performance evaluation of specificity

**Figure 7:** Performance evaluation of sensitivity

Figure 6 depicts the specificity evaluation performance. Comparative methods include RF, SVM, KNN, GAN, and proposed methods. We obtained specificity results of 72 percent, 83 percent, 85 percent, 78 percent, and 95 percent using RF, SVM, KNN, GAN, and proposed methods. However, the proposed method outperforms the previous methods in terms of specificity.Figure 7 depicts the performance of the sensitivity evaluation. RF, SVM, KNN, GAN, and proposed methods are examples of comparative methods. Using RF, SVM, KNN, GAN, and proposed methods, we obtained sensitivity results of 78 percent, 84 percent, 87 percent, 89 percent, and 94 percent. However, in terms of sensitivity, the proposed method outperforms the previous methods.

## 5. Conclusion

The work in this article is based on the CGAN-RFO base image quality enhancement over the digital radiography images. The normalization of the images was performed with the Min-Max normalization to perpetuate the detailing and textures. The CGAN overcomes the shortcomings of conventional GAN and thus enhances the image contrast. To attain the optimized output we have adopted the RFO algorithm which optimized the image quality with its

searchability and convergence parameters. Further experiments were conducted and our proposed approach effectively enhances the image quality more than the other approaches. Thus our proposed work can be used to detect the diseases from the radiography images.

## References

**Dr. M. Nagaraju Naik** received his Ph. D from Andhra University College of Engineering (Autonomous), Andhra Pradesh, India, in 2017. Masters Degree in Digital Systems and Computer Electronics (DSCE) from JNTUA, Anantapur, Andhra Pradesh in 2005, and Bachelor of Technology from K. S. R. M. College of Engineering, Kadapa, Andhra Pradesh, in 1999. India, His interest area Signal, Image and Video Processing.

1. Sakib, S., Tazrin, T., Fouda, M.M., Fadlullah, Z.M. and Guizani, M., 2020. DL-CRC: deep learning-based chest radiograph classification for COVID-19 detection: a novel approach. *Ieee Access*, *8*, pp.171575-171589.
2. Tolkachev, A., Sirazitdinov, I., Kholiavchenko, M., Mustafaev, T. and Ibragimov, B., 2020. Deep learning for diagnosis and segmentation of pneumothorax: the results on the kaggle competition and validation against radiologists. *IEEE Journal of Biomedical and Health Informatics*, *25*(5), pp.1660-1672.
3. Ying, X., Wang, L., Wang, Y., Sheng, W., An, W. and Guo, Y., 2020. Deformable 3d convolution for video super-resolution. *IEEE Signal Processing Letters*, *27*, pp.1500-1504.
4. Schenato, L., Pasuto, A., Galtarossa, A. and Palmieri, L., 2020. An optical fiber distributed pressure sensing cable with pa-sensitivity and enhanced spatial resolution. *IEEE Sensors Journal*, *20*(11), pp.5900-5908.
5. Daube-Witherspoon, M.E., Viswanath, V., Werner, M.E. and Karp, J.S., 2020. Performance characteristics of long axial field-of-view PET scanners with axial gaps. *IEEE Transactions on Radiation and Plasma Medical Sciences*, *5*(3), pp.322-330.
6. Dogan, T., de Riet, J., Bel, T., Katsouras, I., Witczak, L., Kronemeijer, A.J., Janssen, R.A. and Gelinck, G.H., 2020. 1000-Pixels per Inch Transistor Arrays Using Multi-Level Imprint Lithography. *IEEE Electron Device Letters*, *41*(8), pp.1217-1220.
7. Wang, J., Sun, K., Cheng, T., Jiang, B., Deng, C., Zhao, Y., Liu, D., Mu, Y., Tan, M., Wang, X. and Liu, W., 2020. Deep high-resolution representation learning for visual recognition. *IEEE transactions on pattern analysis and machine intelligence*, *43*(10), pp.3349-3364.
8. Wu, J., Ma, J., Liang, F., Dong, W., Shi, G. and Lin, W., 2020. End-to-end blind image quality prediction with cascaded deep neural network. *IEEE Transactions on Image Processing*, *29*, pp.7414-7426.
9. Wang, J., Li, J., Yan, S., Shi, W., Yang, X., Guo, Y. and Gulliver, T.A., 2020. A novel underwater acoustic signal denoising algorithm for Gaussian/non-Gaussian impulsive noise. *IEEE Transactions on Vehicular Technology*, *70*(1), pp.429-445.
10. Oh, Y., Park, S. and Ye, J.C., 2020. Deep learning COVID-19 features on CXR using limited training data sets. *IEEE transactions on medical imaging*, *39*(8), pp.2688-2700.
11. Shi, F., Wang, J., Shi, J., Wu, Z., Wang, Q., Tang, Z., He, K., Shi, Y. and Shen, D., 2020. Review of artificial intelligence techniques in imaging data acquisition, segmentation, and diagnosis for COVID-19. *IEEE reviews in biomedical engineering*, *14*, pp.4-15.
12. Eslami, M., Tabarestani, S., Albarqouni, S., Adeli, E., Navab, N. and Adjouadi, M., 2020. Image-to-images translation for multi-task organ segmentation and bone suppression in chest x-ray radiography. *IEEE transactions on medical imaging*, *39*(7), pp.2553-2565.
13. Li, H., Han, H., Li, Z., Wang, L., Wu, Z., Lu, J. and Zhou, S.K., 2020. High-resolution chest x-ray bone suppression using unpaired CT structural priors. *IEEE transactions on medical imaging*, *39*(10), pp.3053-3063.
14. Oyelade, O.N., Ezugwu, A.E.S. and Chiroma, H., 2021. CovFrameNet: An enhanced deep learning framework for COVID-19 detection. *Ieee Access*, *9*, pp.77905-77919.
15. Al-Waisy, A.S., Al-Fahdawi, S., Mohammed, M.A., Abdulkareem, K.H., Mostafa, S.A., Maashi, M.S., Arif, M. and Garcia-Zapirain, B., 2020. COVID-CheXNet: hybrid deep learning framework for identifying COVID-19 virus in chest X-rays images. *Soft computing*, pp.1-16.
16. Shankar, K. and Perumal, E., 2021. A novel hand-crafted with deep learning features based fusion model for COVID-19 diagnosis and classification using chest X-ray images. *Complex & Intelligent Systems*, *7*(3), pp.1277-1293.
17. Karar, M.E., Hemdan, E.E.D. and Shouman, M.A., 2021. Cascaded deep learning classifiers for computer-aided diagnosis of COVID-19 and pneumonia diseases in X-ray scans. *Complex & Intelligent Systems*, *7*(1), pp.235-247.
18. Koonsanit, K., Thongvigitmanee, S., Pongnapang, N. and Thajchayapong, P., 2017, August. Image enhancement on digital x-ray images using n-clahe. In *2017 10th Biomedical engineering international conference (BMEICON)* (pp. 1-4). IEEE.
19. Patro, S. and Sahu, K.K., 2015. Normalization: A preprocessing stage. *arXiv preprint arXiv:1503.06462*.
20. Munkhdalai, L., Munkhdalai, T., Park, K.H., Lee, H.G., Li, M. and Ryu, K.H., 2019. Mixture of activation functions with extended min-max normalization for forex market prediction. *IEEE Access*, *7*, pp.183680-183691.
21. Guo, R., Liu, H., Xie, G. and Zhang, Y., 2021. Weld defect detection from imbalanced radiographic images based on contrast enhancement conditional generative adversarial network and transfer learning. *IEEE Sensors Journal*, *21*(9), pp.10844-10853.
22. Guerrero-Valadez, Juan, and Felix Martínez-Rios. "Rain-Fall Optimization Algorithm with new parallel implementations." EAI Endorsed Transactions on Energy Web 7, no. 29 (2018).
23. Kaboli, S. Hr Aghay, J. Selvaraj, and N. A. Rahim. "Rain-fall optimization algorithm: A population based algorithm for solving constrained optimization problems." Journal of Computational Science 19 (2017): 31-42.
24. Isola, P., Zhu, J.Y., Zhou, T. and Efros, A.A., 2017. Image-to-image translation with conditional adversarial networks. In *Proceedings of the IEEE conference on computer vision and pattern recognition* (pp. 1125-1134).